

Article

Preparation and Tribocorrosion Performance of Different Si-Doped TiSiN-Ag Coatings on Different Substrates in Seawater

Ke Cai ^{1,2}, Bailing Jiang ^{1,*}, Jing Zhang ³ and Xiaolei Su ^{3,*}

¹ School of Materials Science & Engineering, Xi'an University of Technology, Xi'an 710048, China; caike@cnpc.com.cn

² CNPC Tubular Goods Research Institute, Xi'an 710077, China

³ School of Materials Science & Engineering, Xi'an Polytechnic University, Xi'an 710048, China; Zhangjing@xpu.edu.cn

* Correspondence: jiangbail@vip.163.com (B.J.); su_x_lei@163.com (X.S.); Tel.: +86-29-8231-2617 (B.J.)

Abstract: TiSiN-Ag composite coatings with different Si doping contents were prepared by multi-arc ion plating technology on 316L, TC4, and H65 copper substrates, respectively. The microstructure of the prepared coatings was characterized by X-ray diffraction, scanning electron microscopy, and energy-dispersive spectroscopy, respectively. The mechanical properties, electrochemical properties, and tribological properties were characterized by a micro-hardness tester, electrochemical workstation, scratch tester, and friction and wear tester, respectively. Results showed that the coatings with 8 wt.% Si doping content had a smaller average grain size, denser structure, excellent mechanical properties, and better anti-tribocorrosion performance than those with 5 wt.% Si doping content. The coating on the TC4 substrate with 8 wt.% Si doping content presented the best combination of properties and is a candidate for an anti-tribocorrosion material in seawater.

Keywords: TiSiN-Ag coating; tribocorrosion; substrate; Si doping; seawater



Citation: Cai, K.; Jiang, B.; Zhang, J.; Su, X. Preparation and Tribocorrosion Performance of Different Si-Doped TiSiN-Ag Coatings on Different Substrates in Seawater. *Coatings* **2021**, *11*, 459. <https://doi.org/10.3390/coatings11040459>

Academic Editors: JongHyeon Lee and Juan Creus

Received: 15 February 2021

Accepted: 12 April 2021

Published: 15 April 2021

Publisher's Note: MDPI stays neutral with regard to jurisdictional claims in published maps and institutional affiliations.



Copyright: © 2021 by the authors. Licensee MDPI, Basel, Switzerland. This article is an open access article distributed under the terms and conditions of the Creative Commons Attribution (CC BY) license (<https://creativecommons.org/licenses/by/4.0/>).

1. Introduction

Due to the strong corrosiveness, low viscosity, and poor lubricity of seawater environments and the existence of various forms of friction and wear during the operation of mechanical systems, key friction pair components in marine engineering equipment are facing more severe service conditions than those on land. This restricts the service performance of marine engineering equipment [1–3]. Many scholars use various methods to solve this problem by using coatings [4–12]. However, in many methods and materials, the physical and chemical properties of ternary or quaternary composite coatings formed by adding some doping elements to the basis of binary coatings can be improved by changing the microstructure [13–15]. For example, the intergranular slip with lower critical shear stress took place easily in the Si crystals and Si is often used as the solid lubricants [16]. The combination of soft metal Ag and a hard coating can improve its ability to resist brittle failure, refine grain size, and reduce the damage of the corrosion medium to the coating [17,18]. Therefore, TiSiN-Ag coatings formed by combining doped elements Si and Ag with hard TiN coatings can significantly improve the toughness of nanocomposite coatings and exhibit self-lubricating characteristics while maintaining their high hardness. Q Wan et al. [19] found that a TiSiN coating had good corrosion resistance when the Si doping content in the coating was 5 at.%. Yirong Yao et al. [20] found that a TiSiN coating had better tribological behavior than TiN in seawater and reached the best performance when Si doping content was 8 wt.%. However, there are many studies on the effect of Si doping content on the structure and properties of TiSiN coatings. Nevertheless, the effect of Si doping content on the structure and tribocorrosion performance of TiSiN quaternary nitride coatings with a Ag phase is rarely reported.

Therefore, different Si-doped TiSiN-Ag composite coatings on 316L, TC4, and H65 copper substrates were prepared by a multi-arc ion plating method. The microstructure and tribocorrosion performance of the coatings were characterized. The effects of substrate and bias voltage on the microstructure and tribocorrosion performance of the prepared coatings are discussed. The tribocorrosion mechanism is also presented.

2. Materials and Methods

The coatings were deposited by Hauzer Flexicoat F850 multi-arc ion plating equipment. In the experiment, first, 316L, TC4, and H65 copper substrates were degreased and descaled before deposition. The TiSi target and Ag target (purity = 99.5 wt.%, $\Phi 63 \times 32$ mm) were used as the raw materials.

During deposition of the TiSiN-Ag coating, nitrogen gas was used as the nitrogen source. The first layer of TiSiN coating was deposited by the TiSi target. The bias voltage, target current, argon flow, and deposition time were -20 V, 65 A ($\times 6$), 800 sccm, and 10 min, respectively. The second layer of TiSiN-Ag coating was deposited. The bias voltage, target current, argon flow, and deposition time were -20 V, 35 A ($\times 3$), 350 sccm, and 1 min, respectively. The above two coatings were deposited alternately 6 times. The sample table rotated at a speed of 3 r/min. After deposition, the samples were taken out after cooling.

The microstructure (phase structure, surface morphology, energy spectrometry, surface hardness, and adhesion of the prepared coatings), properties (tribological performance, electrochemical corrosion behavior, and profile of wear scar of the prepared coatings), and related equipment are referred to in our previous study [21]. The indenter on the tester was of a 0.2 mm radius and a 120° taper angle. A normal load range of 0–120 N, a scratch length of 5 mm, and a scratching velocity of 6 mm/min were used in the experiments. The preparation of artificial seawater refers to the ASTM D 1141-98 standard, and the specific components are shown in Table 1.

Table 1. Chemical composition of artificial seawater.

Components	Concentration (g/L)	Components	Concentration (g/L)
NaCl	24.530	KCl	0.695
Na ₂ SO ₄	4.090	NaHCO ₃	0.201
MgCl ₂	5.200	KBr	0.101
CaCl ₂	1.160	H ₃ BO ₃	0.027
SrCl ₂	0.025	NaF	0.003

3. Results

Figure 1 shows the XRD patterns of different Si-doped TiSiN-Ag composite coatings on different substrates. Peaks corresponding to the TiN phase, Ag phase, and Ti phase were observed. The generation of the Ti phase was due to the incomplete reactive deposition of the TiSi target on the substrates during evaporation [22]. Compared with the 5 wt.% Si-doped TiSiN-Ag composite coating, all the TiN diffraction peaks of the XRD patterns of all of the 5 wt.% Si-doped TiSiN-Ag composite coatings were weakened. According to the Scherrer equation, the preferred growth direction was weakened, and the generated columnar crystals decreased with the increasing Si doping content. This is because the increasing Si doping content led to the transformation of columnar crystals to TiN nanocrystals coated by the amorphous Si₃N₄ interfacial phase (nc-TiN/Si₃N₄). At the same time, the increasing Si doping content led to the higher hardness and better corrosion and oxidation resistance of the coatings due to the interfacial strengthening effect. However, no peaks corresponding to the Si₃N₄ and TiSi phase were observed because the Si element existed in the form of amorphous Si₃N₄ in the prepared coatings [23,24]. In addition, pure Ag peaks appeared in all XRD patterns, indicating that there were no reactions between Ag and Si, Ag and Ti, or Ag and N [17].

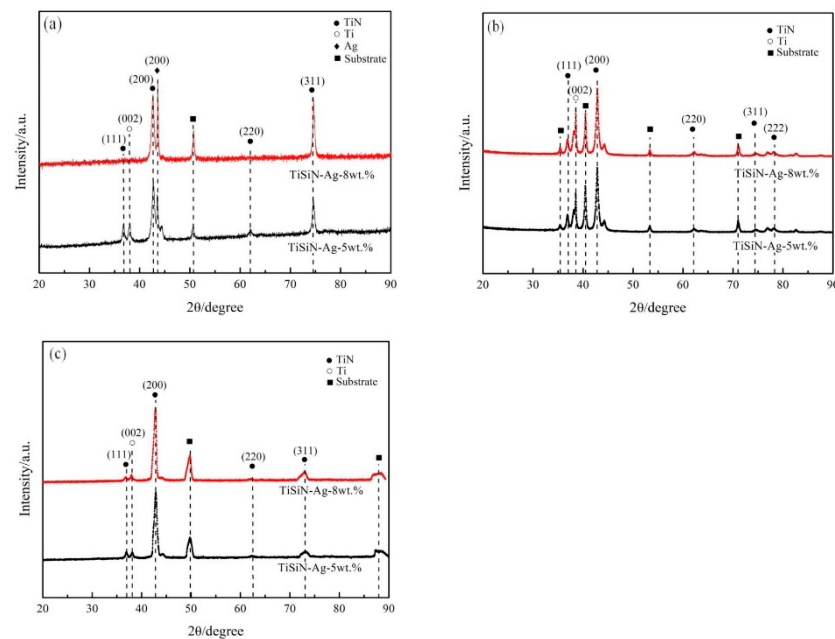


Figure 1. XRD patterns of different Si-doped TiSiN-Ag composite coatings on different substrates: (a) 316L, (b) TC4, (c) Cu.

Figure 2 shows the surface micro-morphologies and cross-sections of different Si-doped TiSiN-Ag composite coatings on different substrates. It could be seen that there were no obvious cracks, pores, or other defects on the surfaces of the coatings, and the large, irregular-shaped crystals were dominant for the TiSiN-Ag composite coatings on the 316L and TC4 substrates. These large particles were evenly distributed. The larger particles could reach more than ten microns and the smaller particles could reach hundreds of nanometers. This was due to the localized evaporation and sputtering of the cathode arc target during deposition [25]. When the Si doping content increased to 8 wt.%, the coating surface became denser, the number of large particles decreased, and the agglomeration of large particles occurred in some areas, which was related to the increase in amorphous phase content [26]. The morphology of the TiSiN-Ag composite coating on the H65 Cu substrate was different from those of the 316L and TC4 substrates. The prepared coatings were vermicular due to the low hardness of the Cu substrate and the high impact of incident particles on the Cu substrate. In addition, it could be seen that the thickness of the coating was approximately 7–8 μm .

Table 2 shows the micro-hardness values ($\text{HV}_{0.3}$) of different Si-doped TiSiN-Ag composite coatings on different substrates. It can be seen that when the Si doping content was 5 wt.%, the average hardness values of the TiSiN-Ag composite coatings on the 316L, TC4, and Cu substrates were $494\text{HV}_{0.3}$, $562\text{HV}_{0.3}$, and $230\text{HV}_{0.3}$, respectively. However, the average hardness of the 8 wt.% Si-doped coatings on the 316L, TC4, and Cu substrates increased to $516\text{HV}_{0.3}$, $588\text{HV}_{0.3}$, and $253\text{HV}_{0.3}$, respectively. This indicates that the micro-hardness of the coating increased slightly with increasing Si doping content. This is because the coating structure was looser, and there was a large gap between grains for the lower Si-doped coatings. When the indenter was pressed and the dislocation had a larger extension space, it showed lower hardness [27]. When the Si doping content increased, more Si atoms dissolved into the TiN lattice and played the role of solid-solution strengthening. In addition, the nc-TiN/ Si_3N_4 composite's structure was formed continuously with increasing Si doping content. The network structure generated by nc-TiN/ Si_3N_4 could effectively hinder crack initiation and propagation, inhibit the growth of crystal grains, and thus effectively improve the hardness of the coating [28,29]. However, relevant studies have shown that the hardness of the coating decreases when the Si doping content increases, up to a certain limit [30,31]. This is because the greater generation of the amorphous Si_3N_4 phases

increases the spacing of TiN columnar crystal clusters, weakening the grain-boundary strength and leading to a decrease in the hardness of the coating. Therefore, there is an optimal Si doping content for TiSiN-Ag composite coatings.

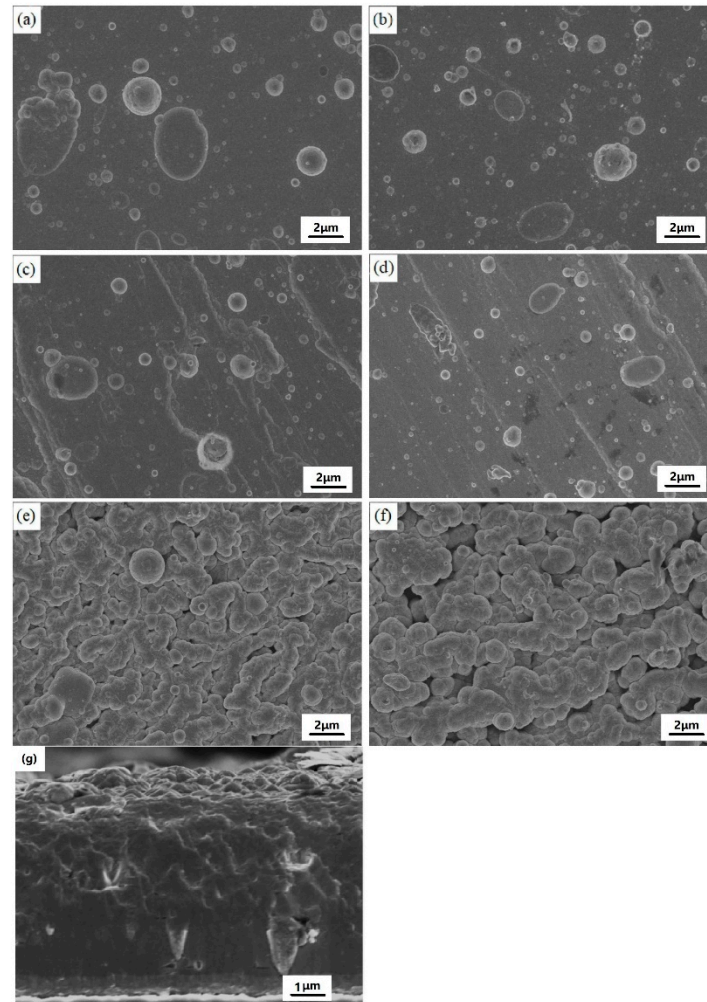


Figure 2. Surface micro-morphologies and cross-section of different Si-doped TiSiN-Ag composite coatings on different substrates: (a) Si-5 wt.%, 316L; (b) Si-8 wt.%, 316L; (c) Si-5 wt.%, TC4; (d) Si-8 wt.%, TC4; (e) Si-5 wt.%, Cu; (f) Si-8 wt.%, Cu; (g) cross-section, Si-8 wt.%, TC4.

Table 2. Micro-hardness values ($HV_{0.3}$) of different Si-doped TiSiN-Ag composite coatings on different substrates.

Substrates	316L		TC4		Cu	
Si doping content (wt.%)	5	8	5	8	5	8
Average micro-hardness ($HV_{0.3}$)	493.83	515.65	561.52	587.64	230.31	252.53

Figure 3 shows scratch test results of different Si-doped TiSiN-Ag composite coatings on different substrates. The scratch length of the coating surface was 5 mm. It could be seen that initial cracks in the 5 wt.% Si-doped TiSiN-Ag composite coating on the 316L and TC4 substrates were 11 N and 20 N, respectively. When the Si doping content increased

to 8 wt.%, the initial cracks increased to 19 N and 72 N, respectively. However, there was no obvious acoustic wave for the TiSiN-Ag composite coating on the H65 Cu substrate, indicating that there was no micro-crack inside the scratch.

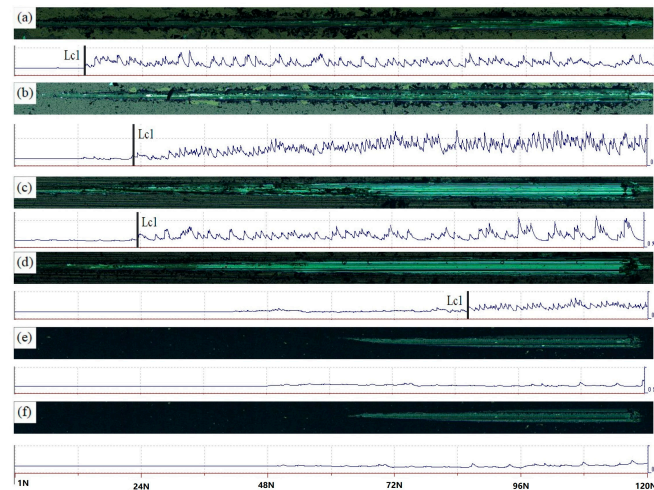


Figure 3. Scratch test results of different Si-doped TiSiN-Ag composite coatings on different substrates: (a) Si-5 wt.%, 316L; (b) Si-8 wt.%, 316L; (c) Si-5 wt.%, TC4; (d) Si-8 wt.%, TC4; (e) Si-5 wt.%, Cu; (f) Si-8 wt.%, Cu.

Compared to the TiSiN-Ag composite coatings with different Si doping content, the adhesion of the coating on the 316L and TC4 substrates increased with increasing Si doping content. This is because increasing the Si doping content improved the solid dissolution enhancement and multi-element enhancement effects. It changed the microstructure and stress-strain distribution of the coating and reduced the mechanical properties and porosity of the coating, increasing the adhesion of the coating [16].

However, related studies [32,33] show that the adhesion of coatings first increases and then decreases with an increase in doping element content. When the Si doping content increases slightly, the large particles on the surface of the coating decrease continuously, which makes many large particles under the compressive stress decrease obviously, and the density of the coating increases. These can effectively inhibit the initiation and expansion of cracks, and the coating's adhesion is continuously improved. When the Si doping content increases to a specific value, excessive stress and cracks inside the coatings are generated easily during the loading process.

Figure 4 shows the open circuit potential (OCP) curves of different Si-doped TiSiN-Ag composite coatings on different substrates. The OCP of the coating before friction was higher, and there was no significant difference in the TiSiN-Ag composite coating with different Si doping content. At the beginning of friction, the OCPs of the coatings decreased significantly. This is because the passivation film had been destroyed due to contact friction on the coating's surface, and the activation area appeared at the wear scar [34]. In the process of friction, the potential always decreases steadily due to the increasing corrosion current density and decreasing corrosion potential, caused by the failure of the passivation film covering the surface of the coating during mechanical wear. This accelerates the corrosion rate [35,36]. The OCPs of the coating increased again at the end of friction. During the friction process, there were small fluctuations in the OCPs of some coatings. This showed that the passivation film was gradually destroyed, and that dissolution and adsorption occurred. Additionally, the potential of different coatings before friction was also similar. Compared with the initial potential of the coatings on the 316L and Cu substrates, the initial potential of the coating on the TC4 substrate was significantly greater, indicating better corrosion resistance. When the Si doping content increased from 5 wt.% to 8 wt.%, the OCPs slightly decreased. This is because the Si atom entered the TiN lattice to generate the solid solution at low Si content and the coating presented the

typical columnar structure. When the Si doping content increased, the nc-TiN/Si₃N₄ phase dispersed more between grains, which reduced the hole defects between grains and made the coating structure denser, thus effectively hindering the penetration of seawater into the coating. Therefore, the corrosion resistance of the coating was effectively improved with increasing amorphous phase content. The 8 wt.% Si-doped TiSiN-Ag coating on the TC4 substrate presented the better corrosion resistance.

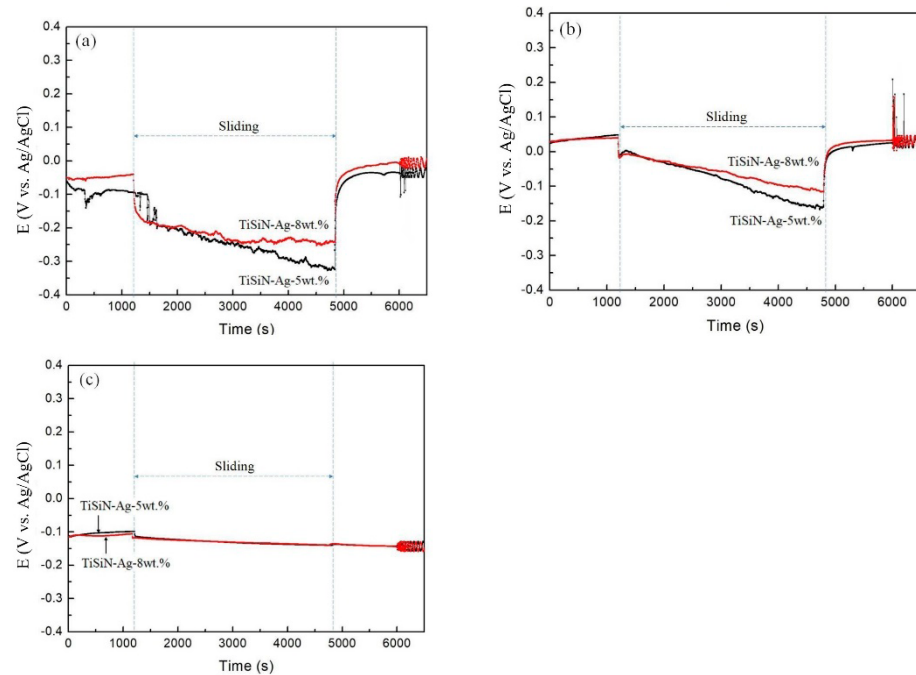


Figure 4. Open circuit potential curves of different Si-doped TiSiN-Ag composite coatings on different substrates: (a) 316L, (b) TC4, (c) Cu.

Figure 5 and Table 3 show dynamic polarization curves and corrosion current density and corrosion potential of different Si-doped TiSiN-Ag composite coatings on different substrates. It can be seen from the figure that the corrosion potential (E_{corr}) and self-corrosion current density (I_{corr}) of the coating on the 316L substrate in a seawater environment were -0.1 V (5 wt.% Si), -0.079 V (8 wt.% Si), 0.07 mA/cm² (5 wt.% Si), and 0.06 mA/cm² (8 wt.% Si), respectively. The corrosion potential and self-corrosion current density on the TC4 substrate were 0.05 V (5 wt.% Si), 0.05 V (8 wt.% Si), 0.0063 mA/cm² (5 wt.% Si), and 0.0013 mA/cm² (8 wt.% Si), respectively. The corrosion potential and self-corrosion current density of the Cu substrate were -0.1 V (5 wt.% Si), -0.1 V (8 wt.% Si), 0.1 mA/cm² (5 wt.% Si), and 0.063 mA/cm² (8 wt.% Si), respectively. Combined with the microstructure analysis of the coatings with different Si doping amounts, the corrosion resistance of the coating with the 8 wt.% doping amount was further improved compared with the coating with the 5 wt.% doping amount. The main reason for this is that the coating with the 8 wt.% doping amount had a denser crystal structure and fewer defects, which greatly hindered the corrosion medium's penetration into the coating and further enhanced the corrosion resistance. Compared with the 316L and Cu substrates, the composite coating based on TC4 had the best corrosion resistance.

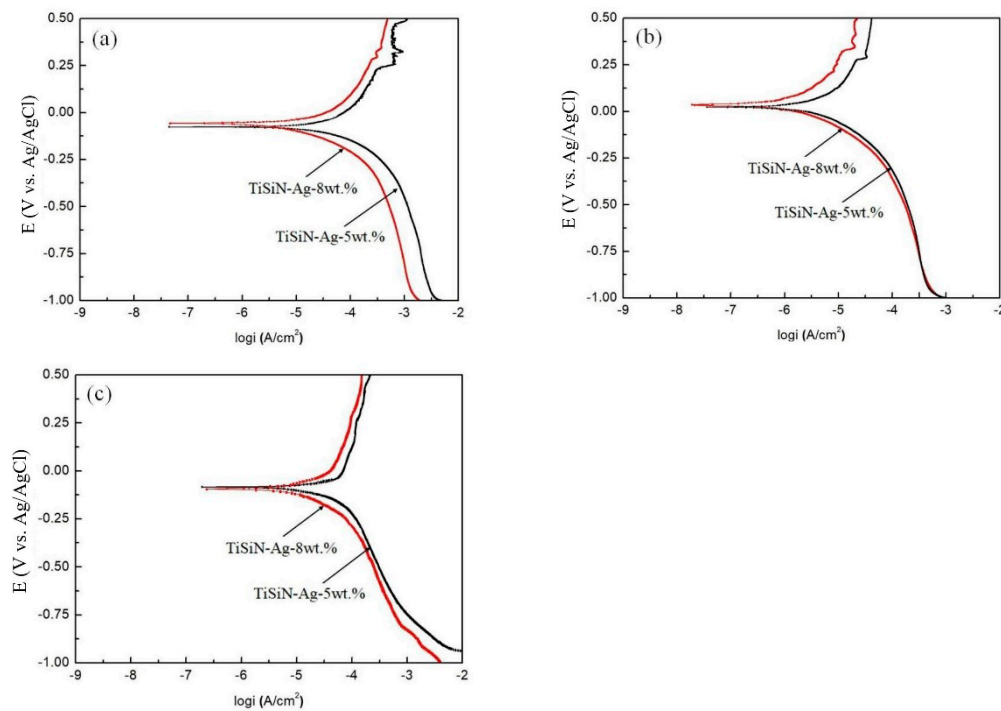


Figure 5. Dynamic polarization curves of different Si-doped TiSiN-Ag composite coatings on different substrates: (a) 316L, (b) TC4, (c) Cu.

Table 3. Corrosion current density and corrosion potential of different materials.

Substrates	316L			TC4			Cu		
	Pure 316L	5	8	Pure TC4	5	8	Pure Cu	5	8
I_{corr} (mA/cm ²)	0.008	0.1	0.079	0.001	0.0063	0.0013	17.404	0.1	0.063
E_{corr} (V)	−0.30	−0.07	−0.06	−0.22	0.05	0.05	−0.347	−0.1	−0.1

Figure 6 shows the friction coefficients of different Si-doped TiSiN-Ag composite coatings on different substrates against Si₃N₄ balls in seawater. When the Si doping content was 5 wt.% and 8 wt.%, the average friction coefficients of the coatings on 316L, TC4, and Cu substrates were 0.51, 0.46, and 0.54, and 0.49, 0.43, and 0.55, respectively. It can be seen that the friction coefficients of 8 wt.% Si-doped TiSiN-Ag coatings on 316L and TC4 substrates were larger than those of the 5 wt.% Si-doped TiSiN-Ag coatings. At the same time, the friction coefficient exhibited less fluctuation and generally maintained a flat trend. This is because: (1) when the Si doping content increased from 5 wt.% to 8 wt.%, a more nanocrystalline composite structure (nc-TiN/Si₃N₄) was generated, which decreased adhesion of coating on substrates and shear stress in the friction process. In addition, the more nanocrystalline composite phase also made a more compact coating structure, resulting in a reduction in the plastic deformation of the coating during friction. (2) The amorphous SiO₂ was generated by tribochemical reaction during the friction process, which dissolved in the seawater solution and formed a thin boundary lubrication film between the friction interfaces, thus reducing the friction coefficient [37,38]. The reactions are as follows:



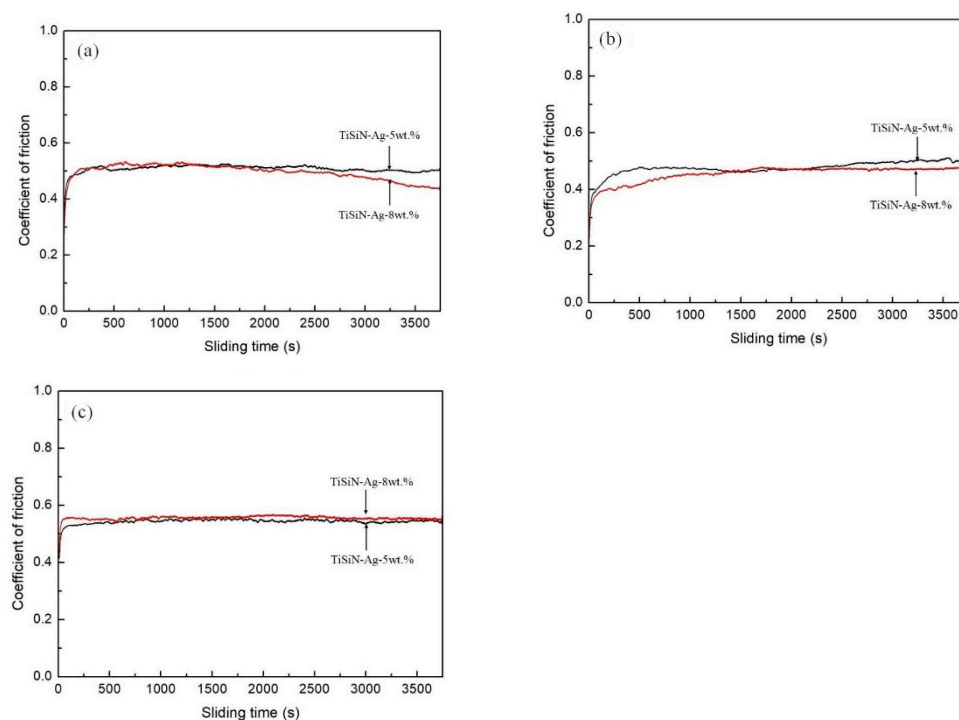


Figure 6. Friction coefficient of different Si-doped TiSiN-Ag composite coatings on different substrates against Si_3N_4 balls in seawater: (a) 316L, (b) TC4, (c) Cu.

However, the friction coefficient of the 8 wt.% Si-doped TiSiN-Ag coating on the Cu substrate was larger than that of the 5 wt.% Si-doped TiSiN-Ag coating. For the samples with low Si-doping content, there are no obvious large particles on the coating's surface. This decreased the number of large ruptured particles under compressive stress significantly and increased the density of the coating continuously. These factors could effectively reduce the friction coefficient. However, when the Si doping content increased to a threshold value, the larger internal stress of the coating easily generated cracks in the friction process. Related studies showed similar results [39,40]. In addition, the ductility and low shear strength of the soft metal Ag phase also played a role in lubrication, which reduced the friction coefficient of the TiSiN-Ag composite coating [17,18].

In order to better illustrate the tribological properties of TiSiN-Ag composite coatings, wear track profiles were introduced. Figure 7 shows the wear track profiles of different Si-doped TiSiN-Ag composite coatings on different substrates against Si_3N_4 balls in seawater. When the Si doping content was 5 wt.%, the wear scar width and depth of coatings on 316L, TC4, and Cu substrates were around 0.605 mm and 2.329 μm , 0.448 mm and 2.195 μm , and 0.566 mm and 3.162 μm , respectively. However, when the Si doping content was 8 wt.%, the wear scar width and depth were around 0.482 mm and 2.149 μm , 0.367 mm and 1.986 μm , and 0.519 mm and 4.174 μm , respectively. It can be seen that fluctuations appeared in the center of the wear track profile. This shows that adhesive wear of the coatings took place during the friction process. Figure 8 shows the wear rate of TiSiN-Ag composite coatings with different Si doping content on different substrates against Si_3N_4 balls in seawater. Because the coatings on the Cu substrate were worn through, the wear rate is not presented. When the Si doping content was 5 wt.%, the wear rates of coatings on the 316L and TC4 substrates were around $9.7850 \times 10^{-6} \text{ mm}^3/(\text{N}\cdot\text{m})$ and $6.8289 \times 10^{-6} \text{ mm}^3/(\text{N}\cdot\text{m})$, respectively. When the Si doping content was 8 wt.%, the wear rates of coatings on the 316L and TC4 substrates were around $7.1933 \times 10^{-6} \text{ mm}^3/(\text{N}\cdot\text{m})$ and $5.0617 \times 10^{-6} \text{ mm}^3/(\text{N}\cdot\text{m})$, respectively. Obviously, the wear rates of the 5 wt.% Si-doped coatings were significantly higher than those of the 8 wt.% doped coatings. This was because the columnar crystals' structure in the 5 wt.% Si-doped coatings could provide diffusion channels for the corrosive medium, weaken the bonding effect of the coating,

and accelerate wear. However, the number of columnar crystal structures in the 8 wt.% Si-doped coatings was small, which could effectively hinder crack growth and decrease the wear rate. In addition, the wear rate of the coating on the TC4 substrate was lower than that of the 316L substrate. This was because as TC4 belongs to a dual-phase alloy, the crystal density was much greater than that of 316L, and its specific strength was higher. When the corrosive medium entered the crystal through the wear scar to reach the interface between the substrate and coating, the faster diffusion rate was the cause of serious damage and even peeling of the coating on the 316L substrate. In the process, the soft Ag could block the continuous growth of the columnar crystal of the coating and refine the grains, reducing the damage of the corrosion media to the coating. Moreover, the combination of the soft Ag phase and the high hardness TiSiN layer could reduce the hardness and elastic modulus of the TiSiN layer, improve its ability to resist brittle damage, and play a lubrication role in the friction process.

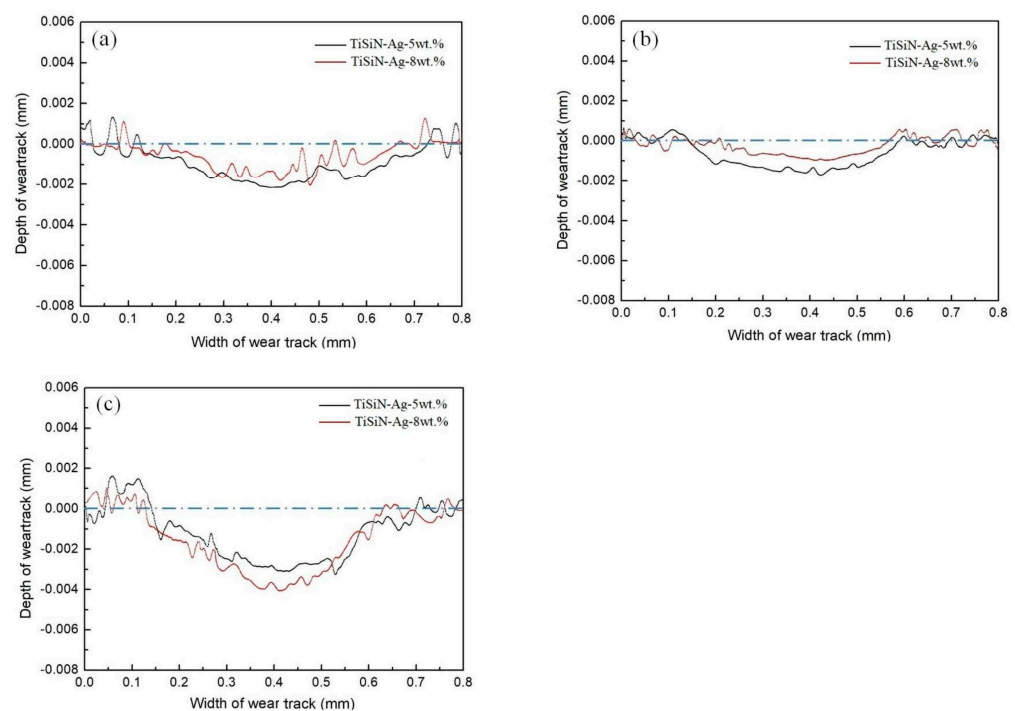


Figure 7. Wear track profiles of different Si-doped TiSiN-Ag composite coatings on different substrates against Si_3N_4 balls in seawater: (a) 316L, (b) TC4, (c) Cu.

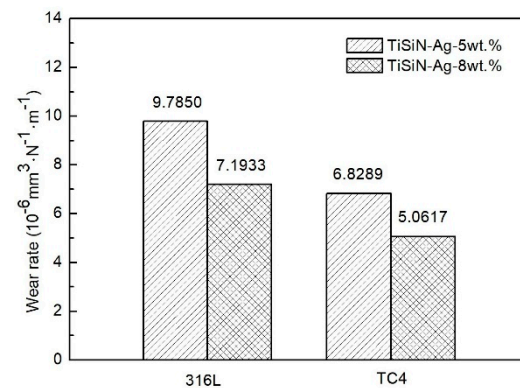


Figure 8. Wear rates of different Si-doped TiSiN-Ag composite coatings on different substrates against Si_3N_4 balls in seawater.

In order to further study the mechanism of friction and wear of TiSiN-Ag composite coatings with different Si doping content on different substrates in seawater, the wear scar

morphologies of different Si-doped TiSiN-Ag composite coatings on different substrates against Si_3N_4 balls in seawater are shown in Figure 9. The coatings on the 316L and TC4 substrates were smooth and flat. There was no peeling or obvious micro-pores in the surface, though flattened furrows were observed. This indicates that the wear mechanism of the coating was a combination of adhesive wear and plastic deformation. Compared with different Si-doped coatings on the same substrate, the wear scar area and width of 8 wt.% Si-doped coatings were less than those of the 5 wt.% Si-doped coatings due to its denser microstructure [41]. In this process, the Si_3N_4 ball was also prone to hydration reaction, which could alleviate the cutting effect of abrasive particles and reduce the wear rate. Meanwhile, white salt crystals with uneven distribution and different sizes attached to the coating surface could be observed, which was caused by the viscosity of seawater and the precipitation of calcium and magnesium salts.

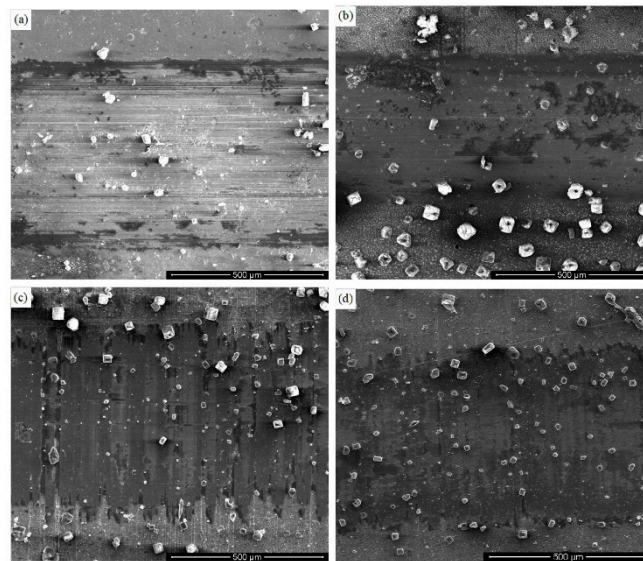


Figure 9. Wear scar morphologies of different Si-doped TiSiN-Ag composite coatings on different substrates against Si_3N_4 balls in seawater: (a) Si-5 wt.%, 316L; (b) Si-8 wt.%, 316L; (c) Si-5 wt.%, TC4; (d) Si-8 wt.%, TC4.

Figure 10 shows the EDS of friction marks of different Si-doped TiSiN-Ag composite coatings on different substrates against Si_3N_4 balls in seawater. Besides the composition of the substrate material and the coating itself, the existence of the O element at the wear mark indicates that oxidation occurred during the friction process. In addition, it can be seen that elements such as Na, Mg, Al, and Cl in the seawater environment settled to the wear marks, and the $\text{Mg}(\text{OH})_2$ and $\text{Al}(\text{OH})_3$ formed during the friction process were also good lubricating media.

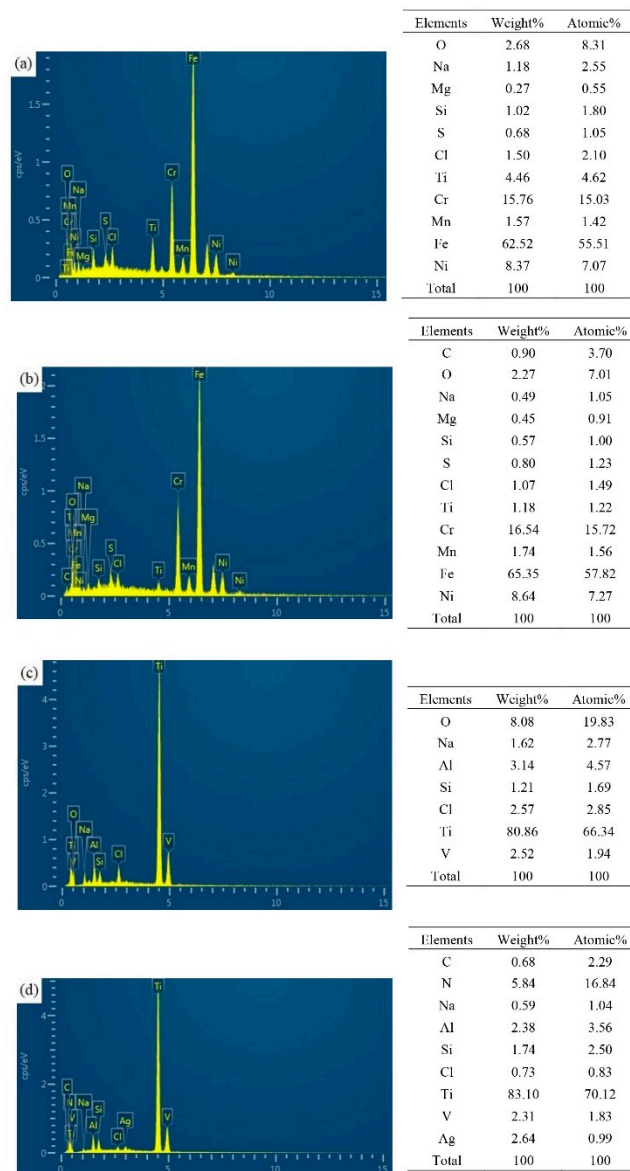


Figure 10. EDS of friction marks of different Si-doped TiSiN-Ag composite coatings on different substrates against Si_3N_4 balls in seawater: (a) Si-5 wt.%, 316L; (b) Si-8 wt.%, 316L; (c) Si-5 wt.%, TC4; (d) Si-8 wt.%, TC4.

4. Conclusions

TiSiN-Ag composite coatings with different Si doping content on different substrates were prepared by multi-arc ion plating technology. The microstructure (phase structure, surface morphology, energy spectrometry, surface hardness, and adhesion), and properties (tribological performance, electrochemical corrosion behavior, and profile of wear scar) were characterized. Compared with 5 wt.% Si-doped TiSiN-Ag composite coatings, the 8 wt.% Si-doped TiSiN-Ag composite coatings had smaller average grain size, more compact structures, higher hardness and adhesion, better tribological properties, and larger OCPs and slope of the anodic polarization curve in the friction. The main reason for this is that there are many nanocrystalline composite structures of amorphous Si_3N_4 interfacial, phase-wrapped nanocrystalline TiN phases (nc-TiN/ Si_3N_4) in 8 wt.% Si-doped TiSiN-Ag composite coatings. The generated network structure can effectively hinder the generation and expansion of coating cracks. Moreover, increasing Si doping content can also reduce the influence of pinholes, cracks, and other defects in the coating due to the interfacial

enhancement effect. The 8 wt.% Si-doped TiSiN-Ag composite coatings on the TC4 substrate presents good anti-tribocorrosion performance in artificial seawater.

Author Contributions: Writing—original draft preparation, K.C.; data curation, J.Z.; writing—review and editing, B.J. and X.S. All authors have read and agreed to the published version of the manuscript.

Funding: This research received no external funding.

Institutional Review Board Statement: Not applicable.

Informed Consent Statement: Not applicable.

Data Availability Statement: The data presented in this study are available on request from the corresponding author.

Conflicts of Interest: The authors declare no conflict of interest.

References

- Di, Q.; Dong, S. Symbiotic state of Chinese land-marine economy. *Chin. Geogr. Sci.* **2017**, *27*, 176–187.
- Ren, W.; Ji, J.; Chen, L.; Zhang, Y. Evaluation of China's marine economic efficiency under environmental constraints—an empirical analysis of China's eleven coastal regions. *J. Clean. Prod.* **2018**, *184*, 806–814. [[CrossRef](#)]
- Abramic, A.; Gonzalez, D.; Bigagli, E.; Che-Bohnenstengel, A.; Smits, P. INSPIRE: Support for and requirement of the marine strategy framework directive. *Mar. Policy* **2018**, *92*, 86–100. [[CrossRef](#)]
- Wail, A.Z.; Muhammad, P.K.; Siti, F.; Nisa, N.; Young, G.K. Recent advances in hybrid organic-inorganic materials with spatial architecture for state-of-the-art applications. *Prog. Mater. Sci.* **2020**, *112*, 100663.
- Wail, A.Z.; Young, G.K. Chemical stability of synergistic inorganic materials for enhancing electrochemical performance. *Compos. Sci. Technol.* **2020**, *199*, 108383.
- Kim, S.-P.; Kaseem, M.; Choe, H.-C. Plasma electrolytic oxidation of Ti-25Nb-xTa alloys in solution containing Ca and P ions. *Surf. Coat. Technol.* **2020**, *395*, 125916. [[CrossRef](#)]
- Wail, A.Z.; Kim, M.J.; Kim, Y.G.; Young, G.K. Dual-functional crosslinked polymer-inorganic materials for robust electrochemical performance and antibacterial activity. *Chem. Eng. J.* **2020**, *392*, 123654.
- Viswanathan, S.S. Superhydrophobic surfaces and coatings by electrochemical anodic oxidation and plasma electrolytic oxidation. *Adv. Colloid Interface* **2020**, *283*, 102245.
- Wail, A.Z.; Dong, K.Y.; Yang, G.K.; Young, G.K. Fabrication of organic-inorganic hybrid materials on metal surface for optimizing electrochemical performance. *J. Colloid Interface Sci.* **2020**, *573*, 31–44.
- Ting, W.; Carsten, B.; Mikhail, L.Z. Influence of secondary phases of AlSi9Cu3 alloy on the plasma electrolytic oxidation coating formation process. *J. Mater. Sci. Technol.* **2020**, *50*, 75–85.
- Wei, K.; Zhang, Y.; Yu, J.; Liu, R.; Du, J.; Jiang, F.; Xue, W. Analyses of hydrogen release on zirconium alloy anode during plasma electrolytic oxidation. *Mater. Chem. Phys.* **2020**, *251*, 123054. [[CrossRef](#)]
- Wail, A.Z.; Young, G.K. Self-assembly of hierarchical N-heterocycles-inorganic materials into three-dimensional structure for superior corrosion protection. *Chem. Eng. J.* **2019**, *356*, 850–856.
- Tillmann, W.; Momeni, S. Tribological development of TiCN coatings by adjusting the flowing rate of reactive gases. *J. Phys. Chem. Solids* **2016**, *90*, 45–53. [[CrossRef](#)]
- Li, J.L.; Cai, G.Y.; Zhong, H.S.; Wang, Y.X.; Chen, J.M. Tribological properties in seawater for Ti/TiCN coatings on Ti6Al4V alloy by arc ion plating with different carbon contents. *Rare Metals* **2017**, *36*, 858–864. [[CrossRef](#)]
- Blinkov, I.V.; Volkhonskii, A.O.; Belov, D.S.; Sergevnikov, V.S.; Chernogor, A.V. Influence of ion energies on the structure, composition, and properties of multilayer Ti-Al-Si-N ion-plasma-deposited coatings. *Tech. Phys. Lett.* **2016**, *42*, 528–531. [[CrossRef](#)]
- Tyagi, R.; Xiong, D.S.; Li, J.; Dai, J. Elevated temperature tribological behavior of Ni based composites containing nano-silver and hBN. *Wear* **2010**, *269*, 884–890. [[CrossRef](#)]
- Mulligan, C.P.; Gall, D. CrN-Ag self-lubricating hard coatings. *Surf. Coat. Technol.* **2005**, *200*, 1495–1500. [[CrossRef](#)]
- Baraket, M.; Mercs, D.; Zhang, Z.G.; Coddet, C. Mechanical and tribological properties of CrN/Ag and CrSiN/Ag nanoscale multilayers. *Surf. Coat. Technol.* **2010**, *204*, 2386–2391. [[CrossRef](#)]
- Wan, Q.; Ding, H.; Yousaf, M.I.; Chen, Y.M.; Liu, H.D.; Hu, L.; Yang, B. Corrosion behaviors of TiN and Ti-Si-N (with 2.9at.% and 5.0at.% Si) coatings by electrochemical impedance spectroscopy. *Thin Solid Films* **2016**, *616*, 601–607. [[CrossRef](#)]
- Yao, Y.; Li, J.; Wang, Y.; Ye, Y.; Zhu, L. Influence of the negative bias in ion plating on the microstructural and tribological performances of Ti-Si-N coatings in seawater. *Surf. Coat. Technol.* **2015**, *280*, 154–162. [[CrossRef](#)]
- Zhang, J.; Su, X.L.; Shan, L.; Liu, Y.; Zhang, P.; Jia, Y. Preparation and tribocorrosion performance of CrCN coatings in artificial seawater on different substrates with different bias voltages. *Ceram. Int.* **2019**, *45*, 9901–9911. [[CrossRef](#)]
- Tkadletz, M.; Mitterer, C.; Sartory, B.; Letofsky-Papst, I.; Czettel, C.; Michotte, C. The effect of droplets in arc evaporated TiAlTiN hard coatings on the wear behavior. *Surf. Coat. Technol.* **2014**, *257*, 95–101. [[CrossRef](#)]

23. Vaz, F.; Rebouta, L.; Goudeau, P.; Pacaud, J.; Garem, H.; Riviere, J.P.; Cavaleiro, A.; Alves, E. Characterisation of $Ti_{1-x}Si_xN_y$ nanocomposite films. *Surf. Coat. Technol.* **2000**, *133–134*, 307–313. [[CrossRef](#)]
24. Choi, S.R.; Park, I.W.; Kim, S.H.; Kim, K.H. Effects of bias voltage and temperature on mechanical properties of Ti-Si-N coatings deposited by a hybrid system of arc ion plating and sputtering techniques. *Thin Solid Films* **2004**, *447*, 371–376. [[CrossRef](#)]
25. Eriksson, A.; Zhu, J.; Ghafoor, N.; Jensen, J.; Greczynski, G.; Johansson, M.; Hultman, L.; Rosén, J. Ti-Si-C-N thin films grown by reactive arc evaporation from Ti_3SiC_2 cathodes. *J. Mater. Res.* **2011**, *26*, 874–881. [[CrossRef](#)]
26. Veprek, S.; Reiprich, S. A concept for the design of novel superhard coatings. *Thin Solid Films* **1995**, *268*, 64–71. [[CrossRef](#)]
27. Warcholiński, B.; Gilewicz, A.; Ratajski, J.; Kukliński, Z.; Rochowicz, J. An analysis of macroparticle-related defects on CrCN and CrN coatings in dependence of the substrate bias voltage. *Vacuum* **2012**, *86*, 1235–1239. [[CrossRef](#)]
28. Almer, J.; Oden, M.; Hakansson, G. Microstructure, stress and mechanical properties of arc-evaporated Cr-C-N coatings. *Thin Solid Films* **2001**, *385*, 190–197. [[CrossRef](#)]
29. Veprek, S.; Argon, A.S. Mechanical properties of superhard nanocomposites. *Surf. Coat. Technol.* **2001**, *146–147*, 175–182. [[CrossRef](#)]
30. Yazdi, M.; Arab, P.; Lomello, F.; Wang, J.; Sanchette, F.; Dong, Z.; White, T.; Wouters, Y.; Schuster, F.; Billard, A. Properties of TiSiN coatings deposited by hybrid HiPIMS and pulsed-DC magnetron co-sputtering. *Vacuum* **2014**, *109*, 43–51. [[CrossRef](#)]
31. Patscheider, J.; Zehnder, T.; Diseren, M. Structure-performance relations in nanocomposite coatings. *Surf. Coat. Technol.* **2001**, *146*, 201–208. [[CrossRef](#)]
32. Warcholiński, B.; Gilewicz, A.; Kukliński, Z.; Myśliński, P. Arc-evaporated CrN, CrN and CrCN coatings. *Vacuum* **2008**, *83*, 715–718. [[CrossRef](#)]
33. Warcholiński, B.; Gilewicz, A. Effect of substrate bias voltage on the properties of CrCN and CrN coatings deposited by cathodic arc evaporation. *Vacuum* **2013**, *90*, 145–150. [[CrossRef](#)]
34. Fathollahzade, N.; Raeissi, K. Electrochemical evaluation of corrosion and tribocorrosion behaviour of amorphous and nanocrystalline cobalt-tungsten electrodeposited coatings. *Mater. Chem. Phys.* **2014**, *148*, 67–76. [[CrossRef](#)]
35. Naghibi, S.A.; Raeissi, K.; Fathi, M.H. Corrosion and tribocorrosion behavior of Ti/TiN PVD coating on 316L stainless steel substrate in Ringer's solution. *Mater. Chem. Phys.* **2014**, *148*, 614–623. [[CrossRef](#)]
36. Chen, J.; Zhang, Q.; Li, Q.; Fu, S.L.; Wang, J.Z. Corrosion and tribocorrosion behaviors of AISI 316 stainless steel and Ti6Al4V alloys in artificial seawater. *Trans. Nonferrous Met. Soc. China* **2014**, *24*, 1022–1031. [[CrossRef](#)]
37. Zhou, F.; Chen, K.; Wang, M.; Xu, X.; Meng, H.; Yu, M.; Dai, Z. Friction and wear properties of CrN coatings sliding against Si_3N_4 balls in water and air. *Wear* **2008**, *265*, 1029–1037. [[CrossRef](#)]
38. Zhou, F.; Wang, X.; Adachi, K.; Kato, K. Influence of normal load and sliding speed on the tribological property of amorphous carbon nitride coatings sliding against Si_3N_4 balls in water. *Surf. Coat. Technol.* **2008**, *202*, 3519–3528. [[CrossRef](#)]
39. Hu, X.; Han, Z.; Li, G.; Gu, M. Microstructure and properties of Ti-Si-N nanocomposite films. *J. Vac. Sci. Technol. A* **2002**, *20*, 1921–1926. [[CrossRef](#)]
40. Hu, X.; Zhang, H.; Dai, J.; Li, G.; Gu, M. Study on the superhardness mechanism of Ti-Si-N nanocomposite films: Influence of the thickness of the Si_3N_4 interfacial phase. *J. Vac. Sci. Technol. A* **2005**, *23*, 114–117. [[CrossRef](#)]
41. Iordanova, I.; Kelly, P.J.; Mirchev, R.; Antonov, V. Crystallography of magnetron sputtered TiN coatings on steel substrates. *Vacuum* **2007**, *81*, 830–842. [[CrossRef](#)]